ADVANCED HEALTHCARE MATERIALS
www.advhealthmat.de

Overcome the "Buckets Effect": Integration of AIEgens into Proteins for Fluorescence-Enhanced Two-Photon Imaging

Miaozhuang Fan, Zhengzheng Li, Gang Feng, Yibin Zhang, Wenguang Zhang, Chengbin Yang, Yonghong Shao, Changrui Liao, Gaixia Xu, and Zhourui Xu**

Luminogens with aggregation-induced emission characteristics (AIEgens) are considered good options for two-photon (2P) probes, owing to their flexibility of design, heavy-metal-free composition, and resistance to photobleaching. However, the design principles for large 2P absorption cross-section (δ) generally require high coplanarity, strong donor–acceptor (D-A) interactions, and long conjugation, which can severely weaken the brightness of AIEgens at the aggregated state and undermine their potential in 2P fluorescence imaging (2PFI). Exploration of a feasible approach to overcome the "Buckets Effect" of AIEgen-based 2P probes is thus a fascinating yet challenging task. Herein, an AIEgen, namely (Z)-2-(4-aminophenyl)-3-(5-(4-(bis(4-methoxyphenyl)amino)phenyl)thiophen-2-yl)acrylonitrile (MTAA) is designed to have a big δ according to the calculation result and a low fluorescence quantum yield (QY) of 2.2% in dimethyl sulfoxide (DMSO). Impressively, upon integrating into bovine serum albumin (BSA), the protein-sized MTAA@BSA dots exhibit a 25-fold higher fluorescence QY compared to MTAA molecules, contributing to an imaging depth of 818 µm in the brain vasculature. The retention and clearance of MTAA@BSA dots in the liver and kidney are also studied using 2PFI. Overall, this work provides a facile approach to overcome the "Buckets Effect" of AIEgen to generate highly efficient, reliable, and biocompatible 2P probes.

1. Introduction

Two-photon fluorescence imaging (2PFI), which absorbs two near-infrared (NIR) photons to generate fluorescence signals, has come to occupy a prominent place in the field of biomedical research.[1] Compared with conventional one-photon fluorescence imaging, 2PFI has three major advantages, including large imaging depth, high spatial resolution, and long observation time.[2] The merits of 2PFI are attributed to the highly restricted scattered photons in their origin by virtue of the localized generation of nonlinear signals.[3] So far, great strides have been made toward understanding the metabolism,[4] structure,[5,6] and activity[7] in biology science, especially brain science.[8–10]

During the past several years, to facilitate the use of 2PFI in biomedical research, various inorganic[11,12] and organic probes[13] have been developed to seek good multiphoton properties. The imaging potential of 2P probes can be estimated according to the value of 2P action cross-section (2PACS),[14] which is the product of δ and the fluorescence QY. In brief, inorganic probes, such as colloidal semiconductor quantum dots[15] (e.g., CdSe/ZnS, CdSeS/ZnS, $Cd_{1-x}Zn_xS_ySe_{1-y}$), gold nanoparticles and nanoclusters,[12] have been reported with large δ on the order of 10^4 to 10^5 GM (1 GM = 10^{-50} cm^4 s photon^{-1}), laying a solid foundation for 2PFI. However, the concerns about biosafety (such as the leakage of heavy metal ions[16] and the accumulative toxicity[17]) and batch-to-batch consistency[18] limited their further use in biological applications. In contrast, organic probes (e.g., small molecules,[13] semiconducting polymers,[19,20] covalent organic frameworks[21]) with easy modification, well-characterized structures, and heavy-metal-free architectures, are better options to develop versatile, reliable, and safe 2P probes, regardless of their relatively low δ value. However, it should be noted that the optical properties of organic probes are easily deteriorated in a physiological environment owing to the aggregation-caused quenching (ACQ) effect.[22] Organic aggregates with random shapes and sizes in physiological environments could also severely affect their circulation and metabolism inside the body,[23] further undermining their potential in vivo biological applications.

M. Fan, Z. Li, G. Feng, Y. Zhang, W. Zhang, C. Yang, G. Xu, Z. Xu
Guangdong Key Laboratory for Biomedical Measurements and Ultrasound Imaging
School of Biomedical Engineering
Shenzhen University Medical School
Shenzhen University
Shenzhen, Guangdong 518055, China
E-mail: xugaixia@szu.edu.cn; xuzhouray@szu.edu.cn

Y. Shao
College of Physics and Optoelectronic Engineering
Key Laboratory of Optoelectronic Devices and Systems of Ministry of Education and Guangdong Province
Shenzhen University
Shenzhen 518060, China

C. Liao
Guangdong and Hong Kong Joint Research Centre for Optical Fiber Sensors
College of Physics and Optoelectronic Engineering
Shenzhen University
Shenzhen 518060, China

The ORCID identification number(s) for the author(s) of this article can be found under https://doi.org/10.1002/adhm.202301568

DOI: 10.1002/adhm.202301568

The emergence of the aggregation-induced emission (AIE) effect has brought a perfect solution to address the issues in conventional organic materials.[24] In general, luminogens with AIE characteristics (AIEgens) are non-/weakly emissive at a single-molecular state in the organic solvent while highly emissive at aggregated state in water. By further formulating into nanoparticles (NPs) with amphiphilic polymers, the optical and structural stabilities of AIEgens aggregates can be ensured for several weeks even in the biological fluid inside the body.[25,26] Current design principles require organic 2P probes to have relatively strong coplanarity, long conjugation, and enhanced D-A interactions to achieve large δ.[2,13,27] However, it is non-trivial to be accomplished on AIEgens, because the design principles go against the nature of AIE and weaken the fluorescence QY at aggregated state.[28] The highly attenuated QY represents the short piece of wood in the "Buckets Effect", which is decisive to the overall performance of 2P AIEgens. To cope with this challenge, scientists have subtly adjusted the molecular structure of AIEgens and balanced their coplanarity and torsion to achieve good imaging properties.[6,29–31] However, it is a compromising strategy that both the δ and QY are below optimal. Recently, another strategy that adjusted the polarity of the nano-environment around AIEgens has been reported to significantly increase the 2PACS of AIEgens.[32,33] Nevertheless, the additional usage of doping molecules may potentially arouse safety concerns and weaken the application potential. Developing a highly efficient and safe strategy to unleash the full potential of AIEgens in 2PFI is thus an important and meaningful task.

In recent years, a growing interest in enhancing the fluorescence properties of fluorophores (including both ACQ and AIE materials) using proteins has been witnessed and applied in biodetection and bioimaging.[34–40] Different from the typical AIE process in nano-formulations, the luminescence of AIEgens-protein complexes resulted from the strong binding between AIEgens and proteins.[41] In this scenario, the intramolecular motions and the intermolecular interactions of AIEgens were largely restricted and weakened, thereby leading to a largely enhanced fluorescence emission.[42] In this case, AIEgens can be designed with higher coplanarity to boost the δ value, which is a good solution to overcome the "Buckets Effect". Moreover, apart from the materials aspect, the protein-based AIEgen complexes usually possess limited hydrodynamic size,[43] which is not only good for biocompatibility but also beneficial for body clearance.[44–46] Therefore, we have foreseen the great opportunity to combine the merits of AIEgens and proteins to develop highly efficient, reliable, and safe 2P probes.

In this work, AIEgen-protein complexes were successfully prepared via a facile method to enable high-quality 2PFI of brain vasculature, liver, and kidney of a mouse (**Scheme 1**). An AIEgen, namely MTAA, with strong D-A interaction and relatively long conjugation, was designed and synthesized and expected to have big δ and low fluorescence QY values. Interestingly, once integrated into BSA, the as-prepared MTAA@BSA dots exhibited strong fluorescence with a QY value of 55% owing to the strong binding between MTAA and BSA. Such fluorescence enhancement compensates for the shortcoming of AIEgen-based 2P probes and complements the short piece of wood in the "Buckets Effect". Remarkably, a large δ of 779 GM of MTAA@BSA dots has been measured at 920 nm, leading to an imaging depth of 818 μm in the brain after the intravenous injection of a low dosage of 1 mg kg^{-1}. In addition, the protein matrix and limited size endowed MTAA@BSA dots with good biocompatibility and efficient body clearance.

2. Results and Discussion

2.1. Photophysical Properties of MTAA

A large 2PACS is the prerequisite of chromophores for high-quality 2PFI applications. It has been reported that a strong electron pull–push effect and increased conjugation length are desirable for small molecules of D-A structure with large δ.[2] However, these D-A chromophores generally have low QY and are not suitable for biological imaging.[47] Thus, it is of great significance to choose appropriate D, π, and A units to construct D-A molecules with large 2PACS or develop a supplementary strategy to compensate for the QY loss of chromophores.

Therefore, we have designed and synthesized a triphenylamine (TPA)-based D-A luminogen, namely MTAA. Methoxy groups were attached to the TPA group to enhance its electron-donating ability and afford a highly twisted conformation. The thiophene segment was used as a π-bridge and additional D unit to increase the conjugation length and further strengthen the electron-donating ability. An electron-withdrawing cyano group was included on the central π-bridge to possibly enlarge the 2PACS while an aniline group was attached to the A unit to ensure brightness.[48] The synthetic route of MTAA was displayed in Scheme S1 (Supporting Information) and the molecular structure was characterized and verified by ^{1}H NMR, ^{13}C NMR, and high-resolution mass spectroscopies (Figures S1–S6, Supporting Information).

Before the photophysical study of MTAA, time-dependent density functional theory (TD-DFT) calculation was conducted (Figure S7, Supporting Information) using the software Gaussian 09 D.01 based on the B3LYP hybrid functional and 6–31G* basis set. The electron clouds of the highest occupied molecular orbital (HOMO) were mainly located on the TPA and thiophene segment, whereas the electron clouds of the lowest unoccupied molecular orbital (LUMO) were primarily localized on the acceptor moiety. The band gap energy was estimated to be 2.73 eV (Figure S7a, Supporting Information). These results suggested an intramolecular charge transfer (ICT) characteristic of the MTAA molecule. The ΔE_{ST} between the first excited singlet state (S_1) and the second excited triplet state (T_2) was calculated to be 0.0627 eV (Figure S7b, Supporting Information), indicating good potential for photodynamic effect.[49] Furthermore, to evaluate the potential of MTAA for 2PI, its theoretical δ value was calculated using Dalton software based on the B3LYP hybrid functional and 6–31G* basis set. The result showed that a δ of 2090 GM was predicted at 808 nm, laying a solid foundation for 2PI (Table S1, Supporting Information).

The absorption maximum of MTAA in DMSO (**Figure 1**a) was located at 464 nm due to the ICT from the electron-donating group to the electron-accepting group. The solvent effect on its photophysical property was then studied. As shown in Figure S9 (Supporting Information), the absorption and emission spectra of MTAA were mostly bathochromic shifted, whereas the fluorescence intensity was decreased with the increase of the

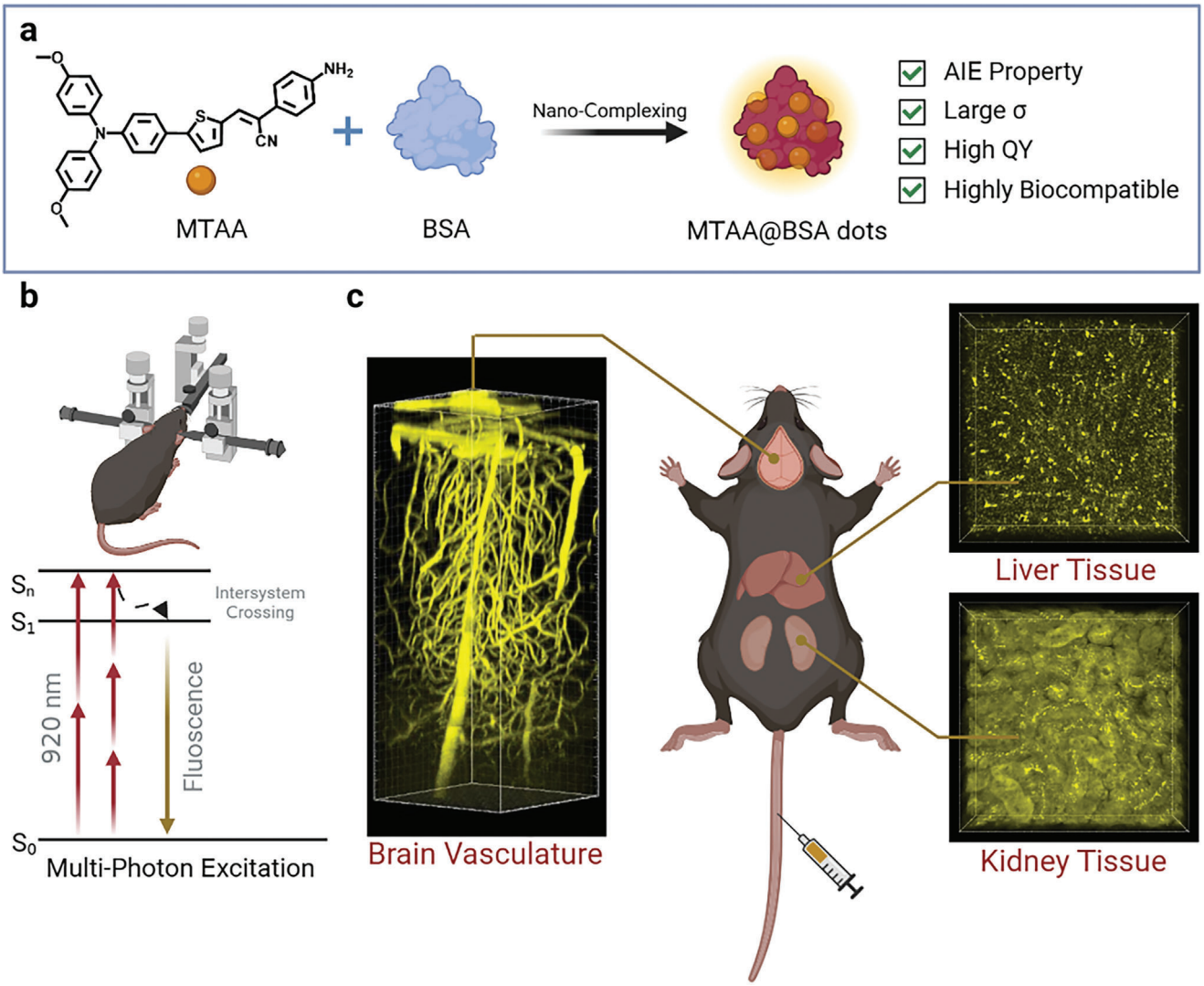

Scheme 1. Schematic illustration of the a) fabrication of MTAA@BSA dots, b) experimental setups for 2P imaging, and c) 2PFI of brain vasculature, liver, and kidney tissues.

solvent polarizability. This phenomenon was ascribed to the transition from the local excitation state to the twisted intramolecular charge transfer (TICT) state.[50,51] Based on the Lippert–Mataga equation,[52] a nearly linear relationship of MTAA between the Stokes shift and the solvent polarity was calculated as 6752 cm^{-1}, indicating a typical TICT effect (Table S2 and Figure S10, Supporting Information). The AIE characteristic of MTAA was then investigated in acetonitrile/water mixtures with varying water fractions (*fw*). As shown in Figure 1b,c, MTAA exhibited a gradually reduced fluorescence emission when the *fw* increased from 0% to 60% due to the strengthening TICT effect, resulted from the increase in solvent polarity. However, in the mixture with larger *fw* the fluorescence intensity of MTAA increased significantly, indicating the AIE property of MTAA. The enhancement of fluorescence intensities was ascribed to the formation of the nano-aggregates, which limited the restriction of intramolecular motion (RIM) of MTAA and thereby enhanced the fluorescence emission. Meanwhile, the twisted conformation of MTAA (optimized by TD-DFT using the B3LYP hybrid functional and 6–31G* basis set) was evidenced by the dihedral angles of 68.34° and 68.44° between the aromatic rings in the TPA unit (Figure S8, Supporting Information), which can efficiently avoid π–π stacking and lead to the AIE tendency.

2.2. BSA-Enhanced Fluorescence Enhancement

To take advantage of the AIE feature of MTAA and render this hydrophobic compound with good water dispersibility and in vivo biocompatibility, DSPE-PEG2000, Pluronic F127, and BSA were used as capping agents to encapsulate MTAA. Interestingly, as shown in **Figure 2**i, MTAA complexed with BSA exhibited highly enhanced (nearly 25-fold and 109-fold) fluorescence intensity compared to those nanoparticles enabled by DSPE-PEG2000 and Pluronic F127. This phenomenon may be attributed to the strong affinity between MTAA and BSA and

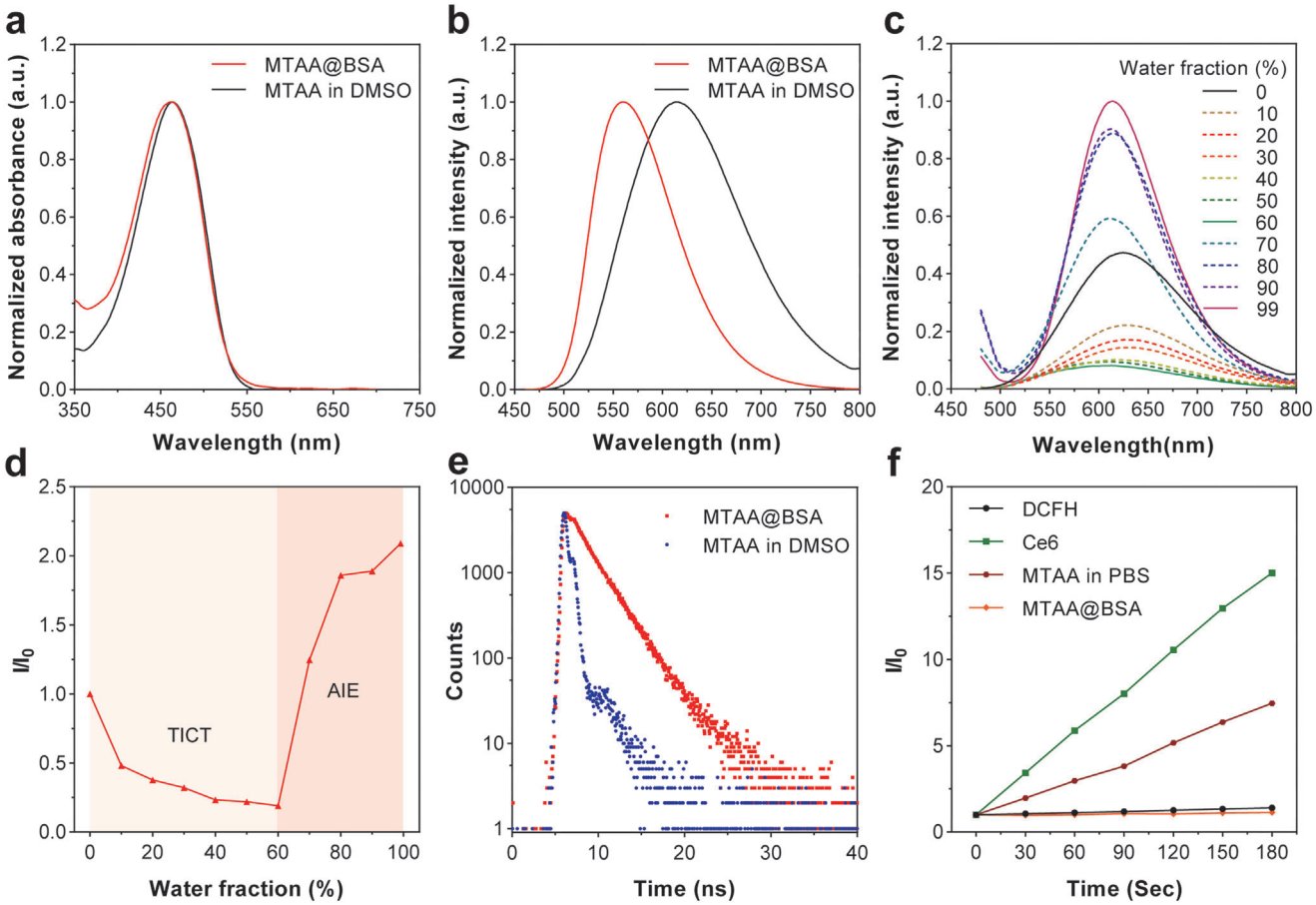

Figure 1. Photophysical properties of MTAA and MTAA@BSA dots. a) UV–vis absorption and b) fluorescence spectra of MTAA@BSA dots and MTAA in DMSO (10 μM). c) Fluorescence spectra and d) the plot of relative emission intensity (I/I_0) of MTAA (10 μM) in acetonitrile/water with different *fw*. e) Fluorescence lifetime of MTAA@BSA dots and MTAA in DMSO (10 μM) under the irradiation of 365 nm light. f) Relative emission intensity (I/I_0) of DCFH in the presence of MTAA in PBS, MTAA@BSA dots, and Ce6 dots (2 μM) upon light irradiation (30 mW cm^{-2}) with different irradiation times.

the highly strengthened RIM. The size and morphology of the MTAA@BSA dots were characterized by dynamic light scattering (DLS) and transmission electron microscopy (TEM), respectively. As shown in Figure 2a–c, and Figure S11a–c (Supporting Information), MTAA@BSA exhibited a hydrodynamic diameter of 13 nm, which was slightly bigger than that of BSA dots (11 nm). In sharp contrast, MTAA aggregates in PBS possessed random shapes with sizes between 500 and 1000 nm. The zeta potential of MTAA@BSA dots was determined to be −8.54 eV, which is similar to those of BSA dots and MTAA aggregates in water (Figure 2d). It should be noted that MTAA@BSA dots exhibited good colloidal stability within 7 days with negligible changes in size distribution and polymer dispersity index (PDI) (Figure 2e,f).

The UV–vis absorption and emission spectra of MTAA@BSA dots in PBS were then measured and compared to those of BSA dots and MTAA aggregates in PBS. As shown in Figure 2g, MTAA@BSA dots contained both the absorption peak of BSA dots and MTAA aggregates. The narrow and slightly blue-shifted absorption peak of MTAA@BSA at 460 nm implied the good dispersity of dots in PBS buffer. In addition, a greatly enhanced fluorescence intensity was observed once MTAA binds to BSA proteins (Figure 2h). The fluorescence peak has a 50 nm blue shift for MTAA@BSA compared to that of MTAA aggregates in PBS. Such fluorescence difference can also be evidenced by the fluorescence images of samples under a UV lamp (inset of Figure 2h). These results implied the successful binding between MTAA and BSA. The average lifetimes of MTAA molecules (in DMSO) and MTAA@BSA dots were characterized using the time-correlated single photon counting (TCSPC) method. As can be seen in Figure 1e, the lifetime of MTAA@BSA dots was obviously longer (2.74 ns) than that (0.76 ns) of MTAA molecules. In contrast to fluorescence emissions, it has been found that the ROS production of MTAA was totally quenched upon the integration into BSA (Figure 1f). This finding is correlate with the enhancement of radiative decay of MTAA.

2.3. Role of BSA in Nano-Formulation

To better understand the role of BSA in nano-formulation, we have carefully adjusted the dosage of DMSO, BSA, and MTAA in the synthesis procedures. Herein, DMSO not only can dissolve MTAA homogenously but also can induce a structural transformation of BSA from the folded to the unfolded state.[53] It is

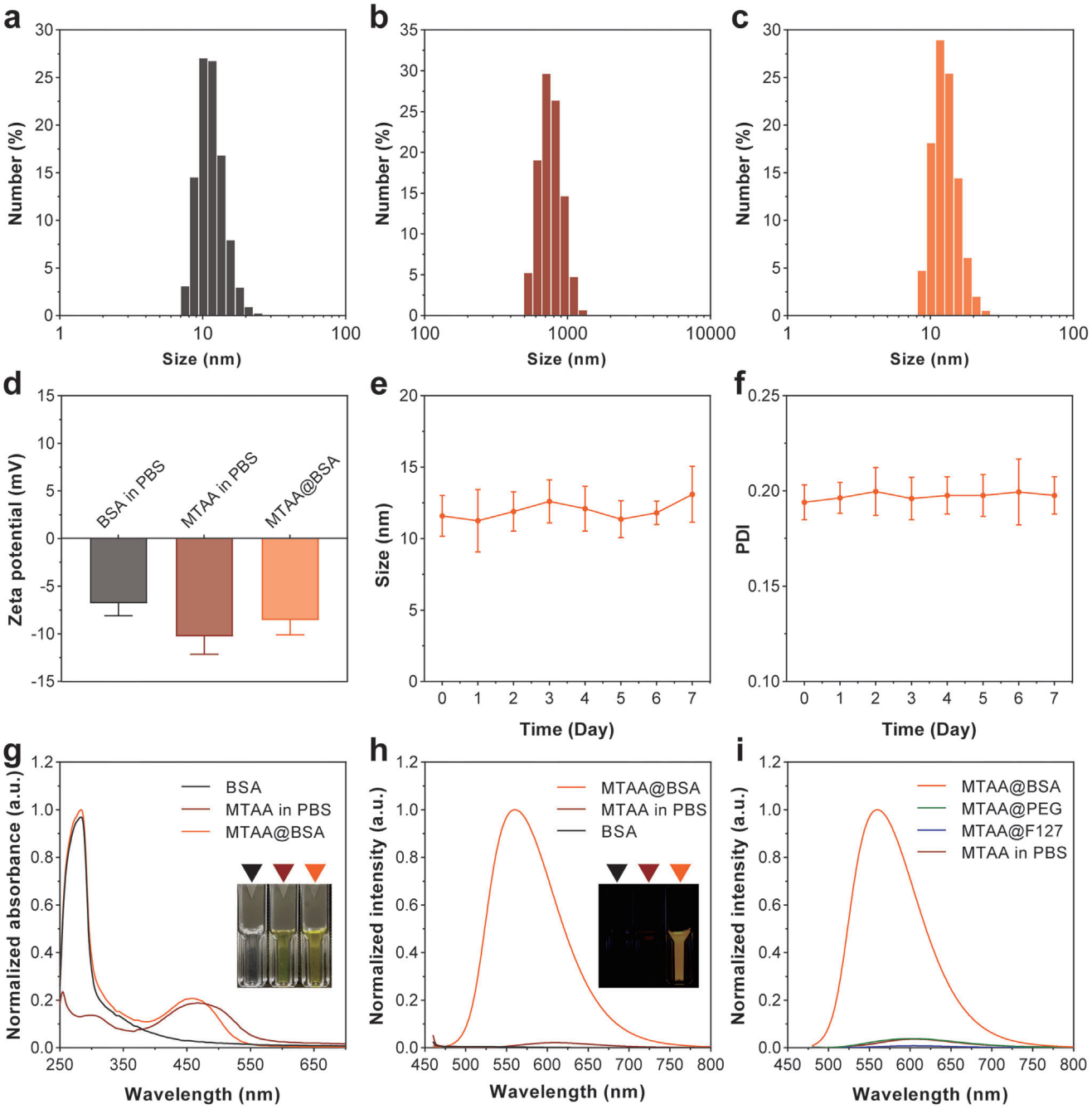

Figure 2. Characterization of MTAA@BSA dots. The Hydrodynamic size of a) BSA in PBS, b) MTAA in PBS, and c) MTAA@BSA dots in PBS. d) Zeta potential of BSA in PBS, MTAA in PBS, and MTAA@BSA dots in PBS. The stability of e) the hydrodynamic size and f) PDI of MTAA@BSA dots in 7 days. g) The absorption and h) fluorescence spectra of BSA, MTAA in PBS, and MTAA@BSA dots. The inset image was captured under white light and UV lamp, respectively. i) Fluorescence spectra of MTAA (10 μM) encapsulated with different matrices. The data with error bar were presented as the mean ± SD ($n = 3$).

believed that the structure of BSA may play a critical role in the formation of MTAA@BSA dots. Thus, the volume ratio of DMSO to BSA was adjusted from 0 to 100% during the dot's fabrication and the fluorescence intensity of MTAA@BSA was characterized. As shown in **Figure 3**a_1,a_2, the fluorescence of MTAA@BSA increased as the volume ratio of DMSO to BSA increased from 0 to 50%; however, the fluorescence was largely weakened at a ratio of 100%. It is assumed that BSA was gradually unfolded in the mixed solvent, which facilitated the interactions between MTAA and BSA. However, such MTAA-BSA bound was not stable in pure DMSO owing to the improved solubility of MTAA. Next, the concentration of BSA was adjusted from 0 to 20 mg mL^{-1} with 50% DMSO during synthesis. As shown in Figure 3b_1,b_2, linear growth of fluorescence enhancement was observed between

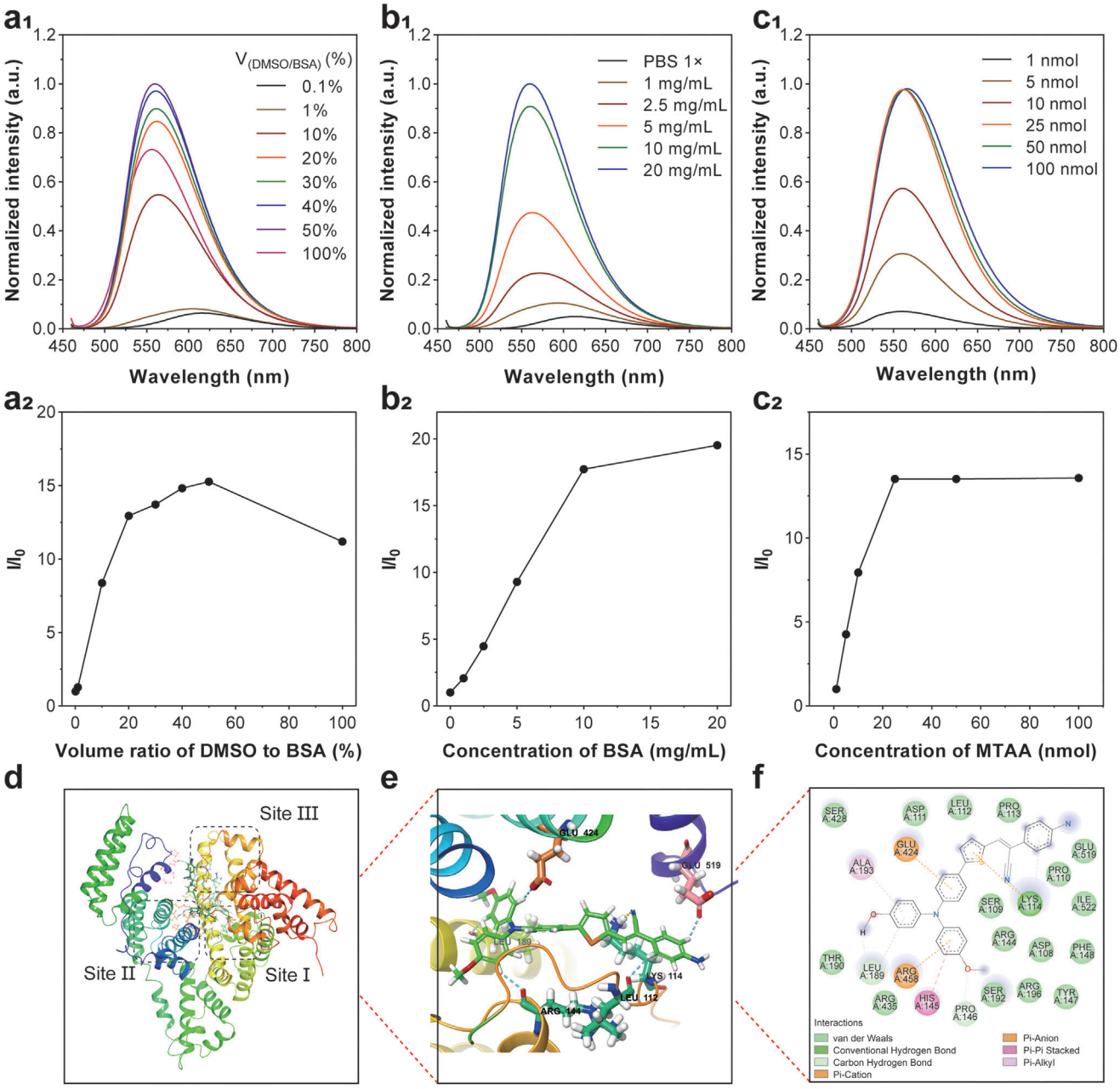

Figure 3. The relationship between MTAA and BSA in the nano-formulation. The fluorescence spectra and the relative emission intensity (I/I_0) of MTAA@BSA dots composited with different a_1,a_2) volume ratios of DMSO to BSA, b_1,b_2) concentration of BSA, and c_1,c_2) concentration of MTAA. d) The binding sites in BSA. e) The hydrophobic pocket of BSA surrounding the MTAA. f) Ligplot of MTAA binding site in BSA.

0 and 10 mg mL^{-1} BSA with a maximum QY of 55%, indicating a good and efficient conjugation between MTAA and BSA. However, only a slight increase of fluorescence enhancement has been observed as the concentration of BSA further increased to 20 mg mL^{-1}. It is assumed that MTAA molecules were mostly exhausted by BSA at 10 mg mL^{-1}, thereby further increasing the BSA would not enhance the fluorescence significantly. To verify this hypothesis, we fixed the concentration of BSA and changed the feeding amount of MTAA in the following test. As shown in Figure 3c_1,c_2, the fluorescence of MTAA@BSA dots continually increased as the feeding quantity of MTAA increased to 25 nmol. Further addition of MTAA did not further increase the fluorescence. Interestingly, under the optimal synthesis parameters of 50% DMSO, 10 mg mL^{-1} BSA (1000 µL), and 1 mM MTAA (25 µL), the molar ratio between BSA and MTAA is very close to 6:1.

In order to clearly illustrate the binding and binding sites of BSA and MTAA, molecular docking was conducted. BSA is a single-chain globular protein[54] that contains three major domains (Sudlow Site I, Sudlow Site II, and Site III),[55] which are

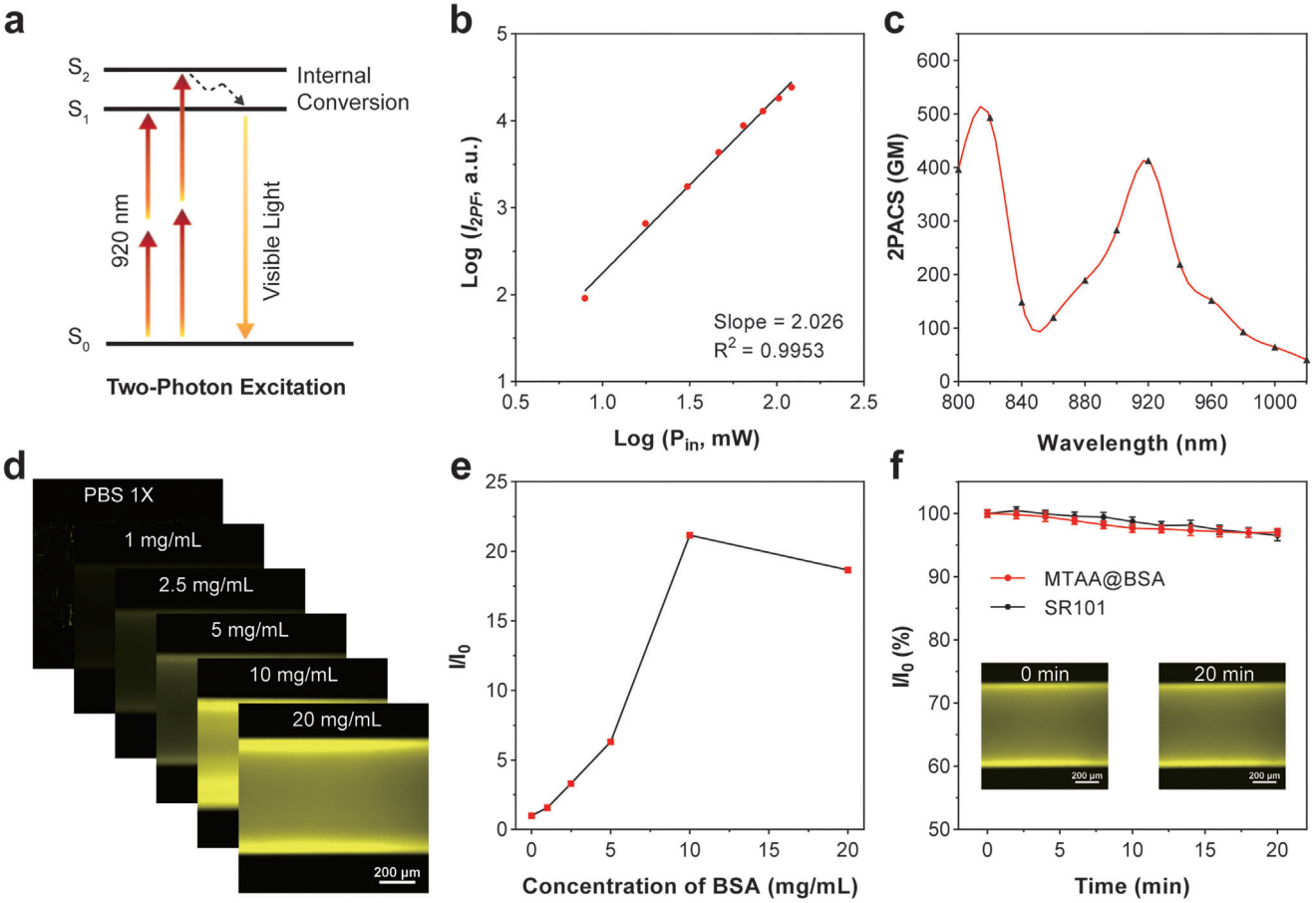

Figure 4. 2P optical properties of MTAA@BSA dots. a) Schematic illustration of fluorescence emission under 2P excitation. b) Measured fluorescence signals versus excitation power for MTAA@BSA dots at the excitation wavelength of 920 nm. c) Measured 2PACS of MTAA@BSA dots from 800 to 1020 nm. d) Fluorescent images excited by a 920 nm fs laser. e) Relative fluorescence intensity of MTAA@BSA dots (10 μM) with different concentrations of BSA. f) Relative fluorescence intensity of MTAA@BSA dots and SR101 under the irradiation of femtosecond laser (920 nm, 50 mW cm^{-2}) for continuous 20 mins (inset: 2P fluorescence images). The data with error bar were presented as the mean ± SD ($n = 3$).

capable to bind almost all known drugs, many nutraceuticals, and toxic substances. As shown in Table S3 (Supporting Information), six identical binding sites for MTAA have been identified based on the simulation results. The number of binding sites is well matched with the molar ratio between BSA and MTAA at the optimal synthesis conditions. Among them, one binding site with a binding constant of −6.896 kcal mol^{-1} located in Site III (Figure S12a, Supporting Information); two binding sites with binding constants of −5.824 and −8.117 kcal mol^{-1} located in Site II (Figure S12b,c, Supporting Information); and another two binding sites with binding constants of −6.716 and −5.314 kcal mol^{-1} located among the Site I to III (Figure 3d,e, and Figure S12d, Supporting Information); only one binding site located closed to the Site I with a binding constant of −7.075 kcal mol^{-1} (Figure S13e, Supporting Information). The force of the molecular binding was constituted by van der Waals forces, hydrogen bond, π–cation, π–anion, π–π stacking, and π–alkyl interactions among different amino acids (Figure 3f). All these interactions helped MTAA to anchor in the Sudlow Site I, Sudlow Site II, and Site III of BSA. Hence, considering the relatively low polarity of BSA, the fluorescence spectrum of MTAA was blue-shifted upon the integration into BSA (Figure 1b). It is thus reasonable to assume that the charge separation of MTAA turn weak, which may enlarge the ΔE_{ST} and undermine its potential for photodynamic effect (Figure 1f). In addition, the strong bindings of BSA could also help to slow down the relaxation of the ICT of MTAA after excitation, thus leading to a longer lifetime (Figure 1e).[56]

2.4. 2P Optical Properties of MTAA@BSA

The reasonable molecular design of MTAA and the fluorescence enhancement strategy of BSA integration have prompted us to study the 2P optical properties of MTAA@BSA dots. A commercial multiphoton microscope (NIKON A1MP) was used for properties characterization. Under the excitation of a 920 nm femtosecond (fs) laser, MTAA@BSA dots can absorb two NIR photons and generate one visible light photon (**Figure 4**a). The power dependence of 2PF intensity of the MTAA@BSA dots on excitation intensity of 920 nm fs laser is plotted in Figure 4b with a calculated slope of 2.026, which is demonstrative of the

main nonlinear optical process of 2P fluorescence. The 2PACS of MTAA@BSA dots were then measured by referring to the fluorescence intensity of standard dye under the same excitation conditions. As shown in Figure 4c, the 2PACS of MTAA@BSA dots peaked at 920 nm with a value of 413 GM. The resistance to photobleaching of the MTAA@BSA dots was studied by recording their fluorescence variation upon continuous laser irradiation at 920 nm. As shown in Figure 4f, MTAA@BSA dots maintained more than 96% of their initial 2PF intensity in PBS after 20 min of irradiation, similar to that of a commercially available sulforhodamine 101 (SR101) dye, implying good stability for long-term bioimaging applications.

2.5. Toxicity Assessment of MTAA@BSA

Although BSA is recognized as a safe and biocompatible substance in the field of drug delivery, considering the relatively high dose of BSA and unknown pharmacokinetics of MTAA, it is necessary to evaluate the toxicity of MTAA@BSA systematically. In brief, cellular experiments, hemolysis, body weight recording, blood biochemistry test, organ coefficients calculation, and histological analysis, were performed according to the methods reported in our previous work.[57] HeLa and MCF-7 cells were first used to investigate the cytotoxicity of MTAA@BSA dots. As can be seen in Figure S13 (Supporting Information), over 95% of cells survived even after 48 h of incubation of MTAA@BSA dots at the concentration of 100 μM (according to the amounts of MTAA), indicating its negligible cytotoxicity. Then, a hemolysis test was conducted to investigate the biocompatibility of MTAA@BSA dots. Remarkably, a hemolysis rate smaller than 4% was observed even at the highest concentration of 200 μM (Figure S14, Supporting Information). This result has proved the excellent bio-inertness of MTAA@BSA dots, which is beneficial for in vivo biological applications.

The in vivo toxicity of MTAA@BSA dots was further studied using female C57 mice. Briefly, dots with 5, 10, and 20 mg kg^{-1} dosages were injected into mice intravenously. The body weight was recorded every day in the overall session of 15 days. As shown in **Figure 5**a, mice treated with MTAA@BSA dots grew steadily and showed a similar trend as the control group, implying negligible systemic side effects of MTAA@BSA dots. On day 15, all mice were sacrificed, and the blood and organ samples were harvested for further tests. As can be seen in Figure 5b, the treated group of mice exhibited slightly increased lung coefficients, which may result in the passive accumulation of MTAA@BSA dots in the lung and the organ burden. Next, blood biochemistry tests were performed. The results indicated no distinct variation among all the indexes, implying a healthy immune system and liver and kidney functions (Figure 5c,f). Furthermore, histology analysis on the major organs, including the heart, liver, spleen, lung, kidney, and brain, was conducted and analyzed by a pathologist. As shown in Figure 5g, no inflammation or abnormalities in organ sections have been observed. In addition, the behavior of mice was studied and compared among different groups. Fifteen days after the injection, we have not observed obvious pathological differences in body shape, weight, eating, defecating, and activity among the control group and treated groups. The above results demonstrated the good safety and biocompatibility of MTAA@BSA.

2.6. Two-Photon Imaging of Cancer Cells, Brain Vasculature, Livers, and Kidney

The above results showed that MTAA@BSA dots have high 2PACS and negligible safety concerns, which encouraged us to explore its capabilities in 2PFI. HeLa and MCF-7 cells were incubated with MTAA@BSA dots for 4 h prior to confocal and 2P fluorescence imaging. As can be seen in Figure S15 (Supporting Information), bright yellow fluorescence appeared around the cell nucleus, demonstrating the intracellular distribution of MTAA@BSA dots. Herein, 2PFI showed similar imaging quality compared to confocal fluorescence imaging regarding cell samples.

C57 mice with a cranial window were further used to assess the performance of MTAA@BSA dots in intravital 2PFI. Briefly, MTAA@BSA dots with a low dosage of 1 mg kg^{-1} was injected into a mouse intravenously. A 920 nm fs laser was focused on brain blood vessels via a water immersion objective (40×, NA: 0.95) for 2P excitation. As shown in Figure S16 (Supporting Information), bright yellow fluorescence originated from MTAA@BSA dots located in brain vasculature at various depths. Both big vessels in the shallow brain region and tiny capillaries in the deep brain can be clearly identified. The three-dimensional (3D) images of brain vasculature were reconstructed according to the two-dimensional (2D) images at a series of depths. According to **Figure 6**a–e, a maximum imaging depth of 818 μm beneath the brain surface was obtained, indicating the good 2P properties of MTAA@BSA dots. In sharp contrast, MTAA@PEG NPs that are the extensively used forms of AIEgen NPs have only contributed to an imaging depth of 514 μm, owing to their low fluorescence QY of 2.7% and low 2PACS of 28 GM (Figure S17). Furthermore, the quality of 2P images of brain vasculature at various depths was investigated according to the signal-to-background ratio (SBR). Line profiles of the fluorescence intensity across blood vessels at 100, 400, and 818 μm imaging depth were plotted in Figure 6f_1-h_1 according to 2P fluorescence images in Figure 6f-h. Especially, SBR values were calculated to be 279, 104, and 27, respectively, well demonstrating the good imaging contrast of MTAA@BSA dots in brain tissue. In addition, careful measurement of the 2D images enabled the quantitative analysis of the full width at half maximum (FWHM) of tiny blood capillaries. Specifically, a capillary with a diameter of 28.6 μm can be well resolved even at an imaging depth of 818 μm. Overall, such imaging performance is comparable to or even better than most of the reported results enabled by other AIEgens NPs considering the imaging depth, the dosage used, and the excitation wavelength comprehensively (**Table 1**).

Although the in vivo toxicity of MTAA@BSA dots has been studied via a series of experiments, it is equally important to understand the clearance and retention of dots in a mouse body after the imaging application. In vivo fluorescence imaging is a widely used approach to study the biodistribution of nanoparticles. As shown in Figure S18 (Supporting Information), MTAA@BSA dots gradually accumulated in the liver, kidney, and lung in the

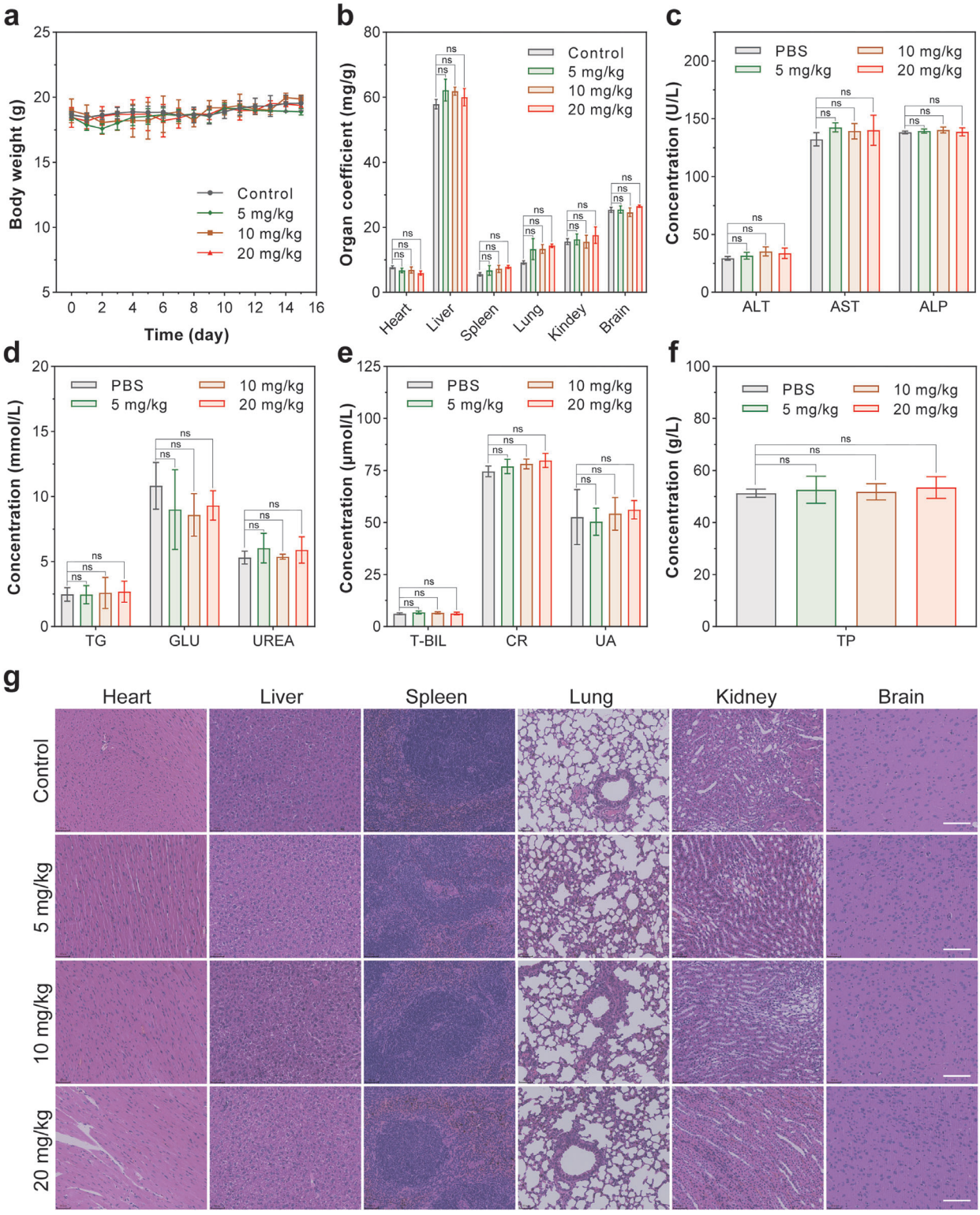

Figure 5. Biotoxicity assessment of MTAA@BSA dots. a) Body weight and b) organ coefficients of mice treated with PBS buffer and different dosages of MTAA@BSA dots. c–f) Blood biochemistry analysis of mice treated with PBS buffer and different dosages of MTAA@BSA dots. (ALT: alanine transaminase; AST: aspartate transaminase; ALP: Alkaline phosphatase; TG: triglyceride; GLU: blood glucose; UREA: blood urea nitrogen; T-Bil: Total bilirubin; CR: Creatinine; UA: Uric acid; TP: Total protein.) g) Histological analysis of the major organs including the heart, liver, spleen, lung, kidney, and brain of mice at the end of 15 days after intravenous injection of MTAA@BSA dots (scale bar is 50 μm). The data with error bar were presented as the mean ± SD ($n = 3$). (Statistics were done using one-way ANOVA for multi-group comparison and unpaired two-tailed Student's *t*-test for two-group comparison. ns, no significance).

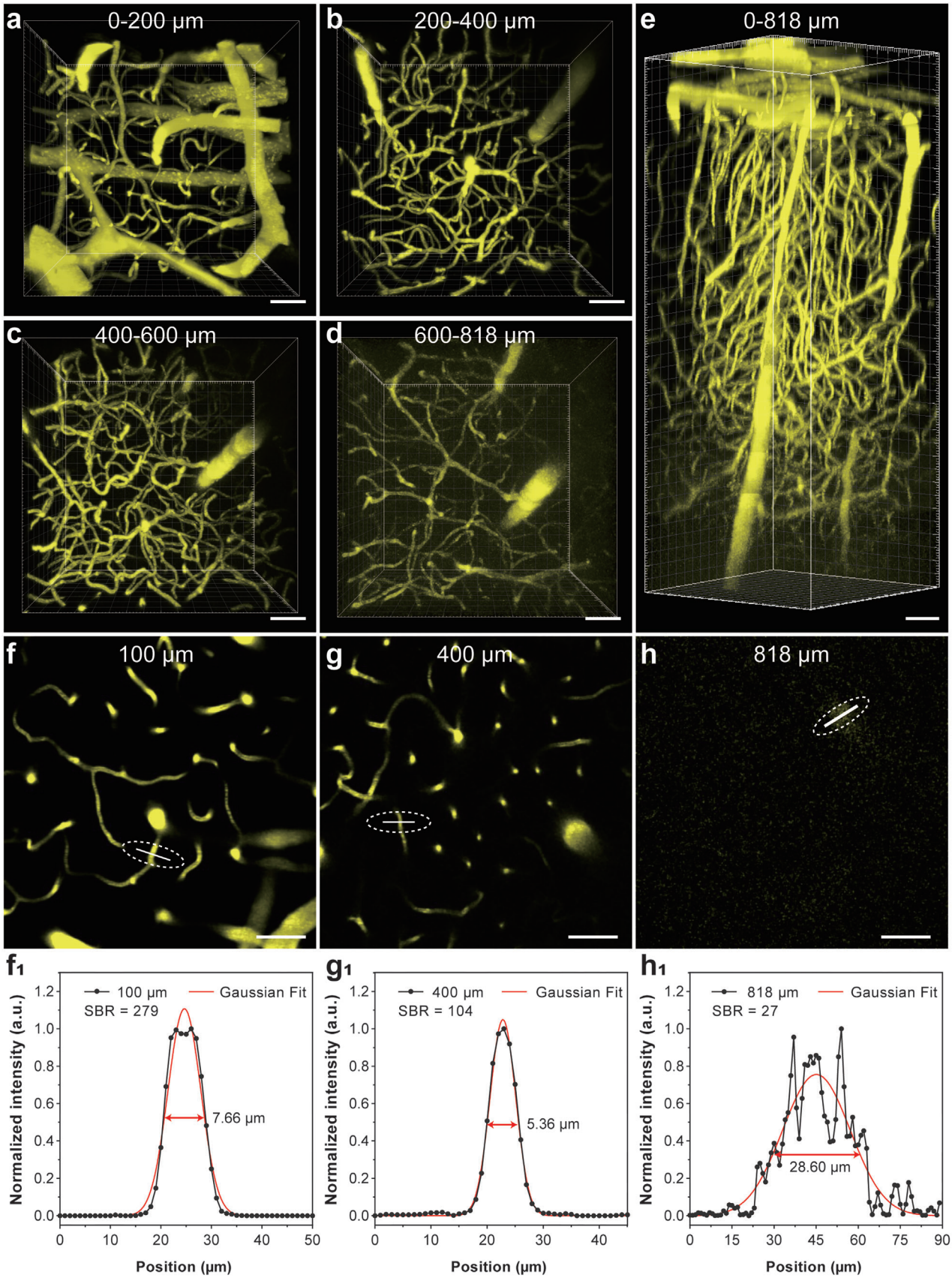

Table 1. The optical properties of AIE NPs and the imaging depth and dosage used in 2PFI.

Name	Matrix	Abs/Em [nm]	QY [%]	δ [GM]	2PEW [nm]	Imaging depth [μm]	Dosage	Reference
TTS	DSPE-PEG2000	497/630	38.5	310	900	225	0.1 mg mL^{-1}, 100 μL	[58]
BTPEBT	DSPE-PEG2000	425/547	62	1.02×10^5	810	424	80 nM, 100 μL	[59]
TPA-BDTO	DSPE-PEG-Mal	523/680	14	1.44×10^5	850	600	0.5 mg mL^{-1}, 100 μL	[60]
TPEPy	FBS	410/640	2	110	840	656	0.25 mg mL^{-1}, 200 μL	[61]
TBP-b-TPA	DSPE-PEG2000	556/690	15.6	207 ± 7	1040	700	1 mg mL^{-1}, 200 μL	[62]
DCCN	Pluronic F127	458/676	12	–	1040	710	1 mg mL^{-1}, 200 μL	[63]
ACIK	Pluronic F127	499/683	5.3	591	1040	800	1 mg mL^{-1}, 200 μL	[64]
AIETP	Pluronic F127	520/620	6	3.1×10^3	1040	800	4.35 nM, 200 μL	[65]
DPTA-BT	DSPE-PEG2000	520/700	9.14	460	1040	802	2 mM, 200 μL	[66]
BTPETQ	DSPE-PEG2000	550/700	19	7.63×10^4	1200	924	0.5 mg mL^{-1}, 100 μL	[67]
TQ-BPN	Pluronic F127	630/810	13.9	1220	1300	1065	1 mg mL^{-1}, 200 μL	[68]
MTAA	BSA	460/560	55	779	920	818	0.1 mg mL^{-1}, 200 μL	This work

Abs, Maximum absorption; Em, Maximum emission; 2PEW, Two-photon excitation wavelength.

first 12 hours followed by hepatic and renal clearance. It should be noted that quite a few MTAA@BSA dots went through renal clearance, which may be attributed to the protein size of the dots. Since the imaging resolution of in vivo fluorescence imaging is relatively low and could not provide detailed information about the internal structure of organs, 2PFI was then applied to the liver and kidney samples. As can be seen in **Figure 7**a-d_1, and Figure S19a-d_1 (Supporting Information), bright yellow tiny dots appeared in the liver cells after 4 hours of injection. At 12 h post-injection, the average fluorescence signals reached the maximum and yellow fluorescence was evenly distributed in liver cells meanwhile big fluorescent aggregates appeared as the intercellular substances. Since then, the fluorescence of the intercellular MTAA aggregates gradually faded away as the indication of hepatic clearance. It is assumed that BSA were firstly catabolized by liver cells and the remaining MTAA molecules were secreted outside the cells and forming large aggregates.[69] Different from the catabolism in the liver, the yellow fluorescence of MTAA@BSA dots was always distributed evenly in the renal tubule and the fluorescence gradually faded away once reached the maximum at 12 hours post-injection (Figure 7g-g_1, and Figure S19g-g_1, Supporting Information). It is believed that the limited size of MTAA@BSA dots can easily pass through the fenestrae (50-100 nm) of capillaries of the glomerulus,[70] thus no large MTAA aggregates have been formed due to the accumulation of MTAA@BSA dots. Overall, the above results clearly showed that the integration of AIEgen into BSA is a facile and feasible strategy to develop highly efficient and safe AIEgen-based 2P probes for 2PFI.

Considering the advantages of in vivo imaging with high signal-to-background ratios, 2PFI has the edge over confocal imaging and small animal fluorescence imaging with regard to monitoring the dynamic biological processes at a sub-organ or cellular level. In the past several years, scientists have developed various organic 2P probes to enable deeper imaging depth in the brain vasculature. We believe it is thus the time to move forward to enable a better understanding of certain diseases by visualizing the whole process of occurring using the 2PFI technique. In this work, MTAA@BSA may offer more possibilities in this aim by taking advantage of proteins, which are related to different biological functions. We hope, based on the experimental results of this work, more innovative works can be encouraged in the future.

3. Conclusion

In this work, protein-sized MTAA@BSA dots were prepared in a facile manner to enable highly efficient and safe 2PFI. A D-A type AIEgen of MTAA with strong D-A interaction, long conjugation, large δ, and relatively low QY was first designed and synthesized. Upon integration into BSA, MTAA@BSA dots have demonstrated a strong fluorescence QY of 55%, which is 25 folds higher than that of MTAA NPs encapsulated by amphiphilic polymers and compensates for the requirements of QY for 2PFI. It has been found that under the optimal condition of dots fabrication, the molecular ratio between MTAA and BSA is 6 to 1, which is well-matched with the number of binding sites inside the BSA. Remarkably, a large imaging depth of 818 μm in the brain vasculature was realized even under a very low dosage of 1 mg kg^{-1} and yellow fluorescence of MTAA@BSA dots, indicating the good 2P properties of MTAA@BSAdots. In addition, the biodistribution of MTAA@BSA dots inside the liver and kidney was examined by 2PFI, which revealed the retention and clearance effects based on sub-organ levels. The safe use of MTAA@BSA has been confirmed by a series of toxicological assessments. Overall, this study provided a feasible and facile approach to combine the merits

Figure 6. Intravital 2PFI of mouse brain vasculature enabled by MTAA@BSA dots. Ex: 920 nm; Filter: 563–588 nm. a–d) 3D reconstructed 2P fluorescence images of mouse brain vasculature at different depth regions. e) 3D reconstructed 2P fluorescence images of mouse brain vasculature network from a depth of 0–818 μm. f–h) 2P fluorescence images of mouse brain vasculature at various vertical depths (100, 400, and 818 μm). f_1–h_1) Fluorescence intensity profiles, SBR analysis, Gaussian Fit, and FWHM analysis of capillary vessel crossed by white line in (f–h). Scale bar: 50 μm.

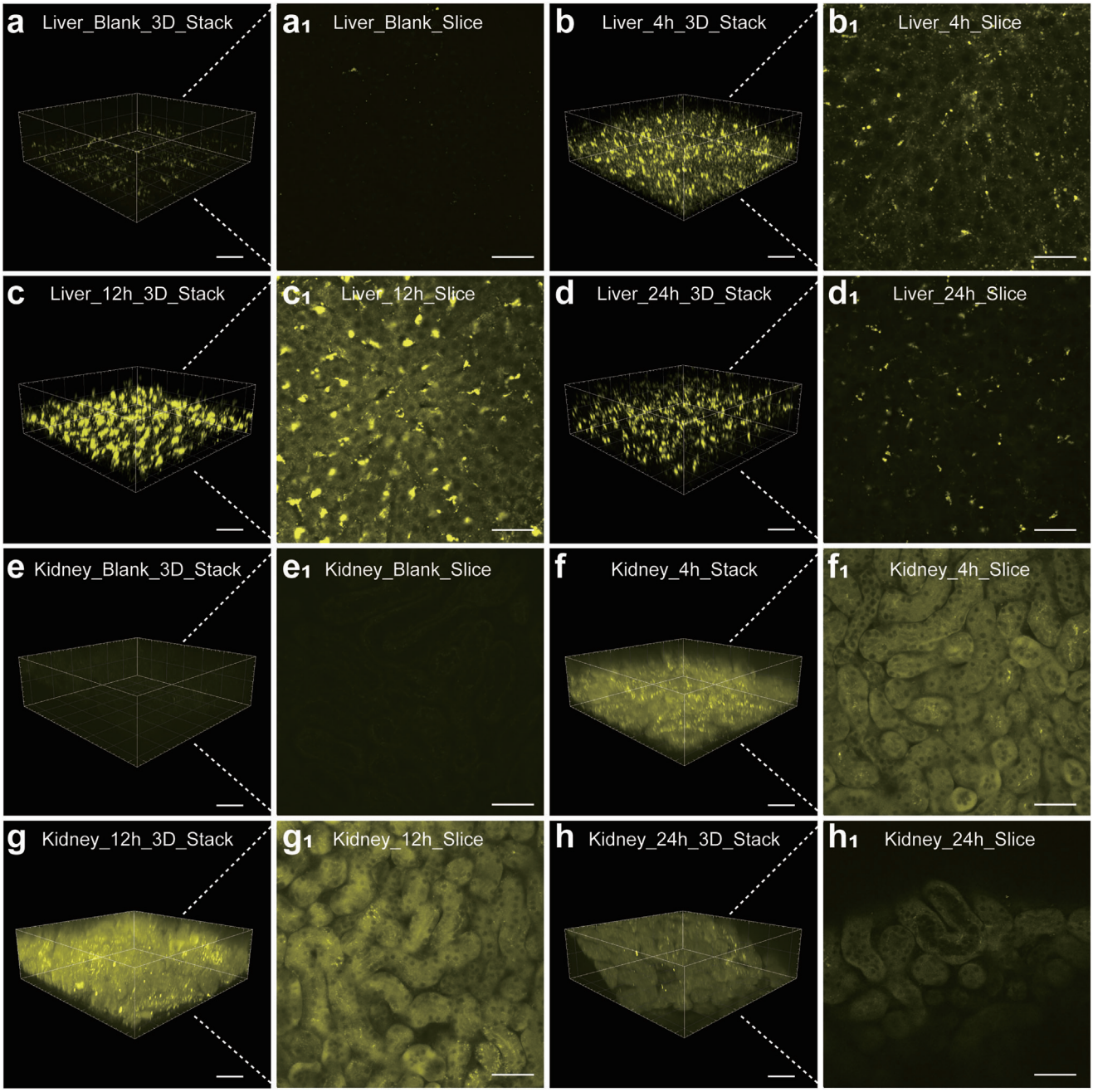

Figure 7. 2P fluorescence images of the mouse (a–d_1) liver and (e–h_1) kidney after being treated with MTAA@BSA dots (200 µL, 1 mg kg^{-1}) for different time duration. Ex: 920 nm; Filter: 563–588 nm. Scale bar: 50 µm.

of AIEgens and proteins and has a great chance of bringing the AIEgen-based 2P probes to the clinical stage of biomedical applications.

4. Experimental Section

Materials and Characterizations: Materials: Distearoyl-sn-glycero-3-phosphoethanolamine-N-[methoxy-(polyethylene glycol)−2000 (DSPE-PEG2000) was purchased from Xi'an ruixi Biological Technology Co., Ltd. Cell counting kit-8 (CCK-8) was purchased from Hangzhou Fude Biological Technology Co., Ltd. Bovine serum albumin (BSA, fatty acid- free) was obtained from Yancheng Saibao Biotech. co. ltd. 2′,7′ -dichlorodihydrofluorescein diacetate (H2DCFDA) was purchased from R&D system, Inc. DMEM medium, fetal bovine serum (FBS), penicillin and streptomycin were purchased from Thermo Fisher Scientific ltd. All organic reagents and chemicals were purchased from Shanghai Macklin Biochemical Co., ltd. All organic reagents and chemicals were used without further purification.

Characterizations: ^{1}H and ^{13}C NMR spectra were measured with Bruker AVANCE III 500 MHz NMR spectrometers using $CDCl_3$ as solvent. High-resolution mass spectra (HRMS) were recorded on XEVO G2-XS QTOF

Mass Spectrometer System operating in a Matrix-Assisted Laser Desorption/Ionization Time of Flight (MALDI-TOF) mode. UV–vis absorption spectra and photoluminescence (PL) spectra were measured on an Agilent 4100 spectrometer and a Hitachi F4600 fluorescence spectrometer, respectively. The hydrodynamic size and zeta potential were characterized using a Malvern Zetasizer Nano-ZS90. The morphologies of nanoparticles were observed on a HITACHI-HT7700 transmission electron microscope (TEM). The cell survival rate was measured using CCK-8 assays and analyzed on a BioTek microplate reader. Fluorescence imaging of mice was conducted on a PerkinElmer IVIS Spectrum. Confocal fluorescence images were captured by a laser scanning confocal microscope ZEISS-LSM880. Two-photon microscope (Nikon-A1MP, 700–1080 nm, pulse width 120 fs, beam diameter 1.2 ± 0.2 mm) was used for the characterizations of 2P properties of nanoparticles and 2PFI.

Synthesis of MTNA: 4-Bromo-N, N- bis(4-methoxyphenyl)aniline (192 mg, 0.5 mmol, 1.0 eq), 5-Formylthiophen-2-boronic acid (234 mg, 0.75 mmol, 2.0 eq), K_2CO_3 (345 mg, 2.5 mmol, 5.0 eq) were added in mixed solvent MeOH/Toluene (v/v = 1: 1). The Pd(dppf)Cl_2 (36 mg, 0.05 mmol, 10 mol%, 0.1 eq) was added into the mixture under N_2 protection. Then, the mixture solution was heated to 75 ^{0}C and kept for 18 h. After 16 h, the mixture solution was filtered to remove the solvent. The reaction residue was further purified by silica gel chromatography using DCM as eluent to obtain the initial product. Then, the initial product (208 mg, 0.5 mmol) and 4-Nitrophenylacetonitrile (81 mg, 0.5 mmol) were dissolved in ethanol with a drop of piperidine. The reaction mixture was refluxed for 5 h followed by cooling down to room temperature and a red product was obtained. The red product was then filtered and washed with cold ethanol and dried in a vacuum to obtain black powder MTNA with a yield of 72%. ^{1}H NMR (500 MHz, Chloroform-*d*) δ 8.29 – 8.26 (m, 2H), 7.80 – 7.74 (m, 3H), 7.63 (d, J = 4.0 Hz, 1H), 7.50 – 7.46 (m, 2H), 7.25 (d, J = 4.0 Hz, 1H), 7.10 (d, J = 8.4 Hz, 4H), 6.90 (d, J = 8.4 Hz, 2H), 6.88 – 6.85 (m, 4H), 3.82 (s, 6H). ^{13}C NMR (126 MHz, $CDCl_3$) δ 156.65, 152.49, 149.95, 147.31, 140.76, 140.04, 137.37, 136.81, 134.98, 127.32, 127.18, 126.00, 124.52, 124.38, 122.44, 119.51, 117.93, 115.01, 103.43, 55.65. HRMS (ESI): m/z calculatedd for $C_{33}H_{25}N_3O_4S$, [M+H]: 560.1599, found 560.1622.

Synthesis of MTAA: MTNA (280 mg, 0.5 mmol) and $SnCl_2{\cdot}2H_2O$ (564 mg, 2.5 mmol) were added into a flask equipped with a magnetic stirrer. Then ethanol (50 mL) was added to the flask. The above mixture was refluxed for 0.5 h followed by cooling down to room temperature. The resulting mixture was neutralized with saturated $NaHCO_3$ to weak basicity (pH = 8), diluted with water (about 50 mL), and extracted with dichloromethane (DCM). The organic phase was then dried over Na_2SO_4 and filtered. The solvent was removed to get a red product. The red product was further purified by recrystallization using hexane and DCM. And then the red solid was dried in a vacuum to obtain red powder MTAA with a yield of 55.41 (m, 6H), 7.17 (d, J = 3.9 Hz, 1H), 7.10–7.06 (m, 4H), 6.93–6.88 (m, 2H), 6.87–6.83 (m, 4H), 6.71 (dd, J = 8.9, 2.5 Hz, 2H), 5.39–5.20 (m, 2H), 3.81 (s, 6H). ^{13}C NMR (126 MHz, $CDCl_3$) δ 156.37, 149.18, 148.45, 147.23, 140.44, 136.41, 133.09, 131.09, 127.06, 126.97, 126.88, 125.42, 124.53, 122.12, 120.08, 118.91, 115.35, 114.94, 106.82, 55.64. HRMS (ESI): m/z calculated for $C_{33}H_{27}N_3O_2S$, [M+H]: 530.1858, found 530.1905.

Fabrication of MTAA@BSA dots: Before synthesizing MTAA@BSA dots, the stock solution of MTAA (1 mM) in DMSO was prepared. BSA powder was dissolved with 1× PBS buffer and filtered by a 0.22 μm filter. Then, MTAA (1 mM) with different volumes of DMSO were added into different concentrations of BSA (1 mL) under vigorous vortex for 30 s, respectively. The mixture was directly used for optical characterization. For MTAA@BSA dots used in biological experiments, the as-prepared MTAA@BSA dots were purified by dialysis (molecular weight cut-off: 100 kDa) against deionized water for a day to remove excessive DMSO and BSA. Then, the purified MTAA@BSA dots were concentrated through ultrafiltration (molecular weight cut-off: 100 kDa) at 4400 rpm for 20 min. The collected MTAA@BSA dots were then dispersed into PBS and filtered by a 0.22 μm filter before being stored at 4 °C in the dark condition.

Measurement of Relative QY: The fluorescence QY (η) of MTAA@BSA dots in water or PBS was characterized using riboflavin as the standard dye (η = 0.3 in basic ethanol, excitation wavelength: 450 nm) according to a fluorescence comparison protocol. In brief, the absorption and emission (under the excitation of 450 nm light) of riboflavin and MTAA@BSA dots were measured. Then, the FL intensities of samples were obtained by spectral integration. Finally, the η value of MTAA@BSA dots was obtained according to the following equation:

$$\eta_1 = \eta_0 \frac{A_0 F_1 n_1^2}{A_1 F_0 n_0^2} \quad (1)$$

where η is QY; A refers to the absorbance at 450 nm; F represents the calculated FL intensity; n refers to the refractive index of the solvent of samples, and the subscripts 1 and 0 represent the MTAA@BSA dots and the standard dye.

Evaluation of ROS Production: The production rate of the overall ROS of MTAA@BSA dots and MTAA in aqueous solution was assessed using the ROS indicator DCFH-DA. DCFH-DA was first activated by sodium hydroxide to produce DCFH. Then, the DCFH solution (40 μM) was mixed with the sample solution (2 μM) homogeneously. Next, the mixed solution containing DCFH and samples was exposed to white light (30 mW cm^{-2}) for 3 min. The fluorescence of DCFH at 525 nm was recorded at a specific time point to indicate the production rate of ROS under the excitation of 488 nm light.

Autodock Simulations: The interaction between MTAA and BSA was conducted by AutoDock simulation. First, the BSA structure was downloaded from the RCSB PDB Protein Data Bank (Crystal Structure of Bovine Serum Albumin PDB code: 4F5S). The software AutoDock Tools 1.5.6 was used to pretreat the BSA structure, which involves removing duplicate protein chains, and water molecules, and then adding hydrogen atoms. Second, the molecular structure of probe MTAA was optimized using DFT calculation by Gaussian09 D.01 at B3LYP/6-31 g (d) level. After that, the docking calculations were performed by the Autodock Vina suite of programs, using a ligand flexible docking approach that allows ligand flexibility. The Lamarckian genetic algorithm was chosen as the search protocol. Finally, the displaying images were performed by Pymol and Discovery Studio.

Characterization of Two-Photon Properties: The two-photon fluorescence (2PF) intensities of MTAA@BSA dots were characterized using a Nikon A1MP multiphoton microscope. The MTAA@BSA dots were loaded in a glass capillary followed by excitation under a fs laser at a wavelength of 920 nm. The 2PF images were then captured via the TRITC channel (563–588 nm). The average 2PF intensities were calculated using ImageJ software and the relationships between the incident laser power and 2PF intensities were plotted.

To measure the two-photon absorption cross-section (δ) of MTAA@BSA dots, rhodamine B in methanol was used as the standard dye. In brief, MTAA@BSA dots and rhodamine B were loaded on glass capillaries, respectively, and then excited by fs laser from 800 to 1020 nm at 20 nm intervals. The 2PF images were captured via the TRITC channel (563–588 nm). The average 2PF intensities were further calculated using ImageJ software. Finally, the σ_2 value of MTAA@BSA dots was obtained according to the following equation:

$$\sigma_{2_1} = \sigma_{2_0} \frac{F_1 \eta_0 c_0 n_0}{F_0 \eta_1 c_1 n_1} \quad (2)$$

where F stands for the 2PF intensity; η for the fluorescence quantum yield; c_0 and $c_1$represent the molar concentration of rhodamine B and MTAA, respectively; n refers to the refractive index of the solvent of samples; and the subscripts 1 and 0 represent MTAA@BSA dots in an aqueous medium and rhodamine B in methanol.

Cell and Culture Conditions: HeLa, and MCF-7 cells were cultured with DMEM medium supplemented with 10% FPS and 1% PS. All cells were cultured in an incubator at 37 °C in a 95% humidified atmosphere containing 5% CO_2.

Confocal Fluorescence Imaging and 2PFI of Cells: HeLa and MCF-7 cells were seeded in confocal cell dishes and cultured to a confluence of nearly 80%. Then, freshly prepared MTAA@BSA dots 200 μM, 10 μL in PBS) were

added to the cell samples for further incubation of 4 h. In addition, the extracellular MTAA@BSA dots were removed by washing the cell samples with PBS. Next, cell samples were imaged using a confocal microscope (ZEISS-LSM880) and/or a 2P fluorescence microscope (NIKON-A1MP). The confocal fluorescence imaging of MTAA@BSA dots was excited by a 458 nm laser and collected within 560–620 nm. The 2PFI of MTAA@BSA dots was excited by a 920 nm fs laser and collected through the TRITC channel (563–588 nm).

Animal Handling: The experimental protocol of animal experiments was approved by the Institutional Ethical Committee of Animal Experimentation of Shenzhen University (Approval NO. AEWC-202300019). Experiments were performed strictly followed by the rules and regulations of governmental and international guidelines on animal experimentation. Female C57 mice were purchased from the Guangdong Medical Laboratory Animal Center and used until 20 g. Before the intravital 2PFI, brain surgery on C57 mice was performed. According to the requirements for Biosafety and Animal Ethics, all efforts were made to minimize the number of animals used and their suffering.

2PFI of Mouse Brain Vasculature: Prior to performing 2PFI of mouse brain vasculature, the mouse was anesthetized using isoflurane and fixed in a stereotaxic frame. During the imaging process, the body temperature of the mouse was kept at 37 °C using a hearing pad. Next, 200 µL of MTAA@BSA dots with a concentration of 0.1 mg mL^{-1} was injected into a mouse intravenously. After 5 min of injection, the mouse was imaged in a two-photon manner. NIKON-A1MP microscope was used to visualize the brain vasculature using a water-immersion objective (40×, NA = 0.95) with 920 nm light. The fluorescence signals of MTAA@BSA dots were collected using the TRITC channel (563–588 nm). The field of view was 318 × 318 µm and each image was acquired every 2 µm in the *z*-axis direction.

2PFI of Mouse Liver and Kidney: Female C57 mice ($n = 3$) were injected with either MTAA@BSA dots (with dosage 1 mg kg^{-1}, 200 µL), and PBS as a control for different duration times, respectively. At different time points, all mice were sacrificed, and the organs were taken. Then, the intact liver and kidney were cleaned with PBS three times, fixed at the bottom of the confocal dish with glue, and then immersed in the surface of the organ with PBS. The 2PFI of mouse liver and kidney were carried out by using a Nikon A1MP multiphoton microscope with a water-immersion objective (40×, NA = 0.95). The fluorescence signals of MTAA@BSA dots were collected using a TRITC channel (563–588 nm). The field of view was 318 × 318 µm and each image was acquired every 2 µm in the *z*-axis direction.

Statistical Analysis: Data were presented as means ± SD. Analyses of experimental data were calculated using GraphPad Prism software (version 9.0) by one-way ANOVA for multi-group comparison and unpaired two-tailed Student's *t*-test for two-group comparison. Statistical analysis was considered significant differences when p values < 0.05. No statistical methods were used to pre-determine the sample size, which was chosen based on prior experience in design.

Supporting Information

Supporting Information is available from the Wiley Online Library or from the author.

Acknowledgements

The authors acknowledge the financial support from the National Natural Science Foundation of China (62205216), Guangdong Natural Science Foundation (2021A1010012159), and Basic Research Foundation of Shenzhen (JCYJ20220531101814003). The authors also thank the Instrument Analysis Centre of Shenzhen University for the equipment used. All animal operations complied with the regulations of the Animal Ethical and Welfare Committee of Shenzhen University (AEWC-SZU).

Conflict of Interest

The authors declare no conflict of interest.

Data Availability Statement

The data that support the findings of this study are available from the corresponding author upon reasonable request.

Keywords

aggregation-induced emission, bovine serum albumin, brain vasculature, fluorescence enhancement, two-photon imaging

Received: May 15, 2023
Revised: July 11, 2023
Published online: August 11, 2023

[1] Z. Xu, Y. Jiang, M. Fan, S. Tang, M. Liu, W.-C. Law, C. Yang, M. Ying, M. Ma, B. Dong, K.-T. Yong, G. Xu, *Adv. Opt. Mater.* **2021**, *9*, 2100859.
[2] M. Fan, Z. Xu, M. Liu, Y. Jiang, X. Zheng, C. Yang, W.-C. Law, M. Ying, X. Wang, Y. Shao, M. T. Swihart, G. Xu, K.-T. Yong, B. Z. Tang, *Appl. Phys. Rev.* **2021**, *8*, 041328.
[3] F. Helmchen, W. Denk, *Nat. Methods* **2005**, *2*, 932.
[4] X. Wang, P. Li, Q. Ding, C. Wu, W. Zhang, B. Tang, *J. Am. Chem. Soc.* **2019**, *141*, 2061.
[5] K. Choe, Y. Hontani, T. Wang, E. Hebert, D. G. Ouzounov, K. Lai, A. Singh, W. Béguelin, A. M. Melnick, C. Xu, *Nat. Immunol.* **2022**, *23*, 330.
[6] S. Wang, J. Liu, C. C. Goh, L. G. Ng, B. Liu, *Adv. Mater.* **2019**, *31*, 1904447.
[7] J. L. Fan, J. A. Rivera, W. Sun, J. Peterson, H. Haeberle, S. Rubin, N. Ji, *Nat. Commun.* **2020**, *11*, 6020.
[8] H. Guan, D. Li, H.-C. Park, A. Li, Y. Yue, Y.-T. A. Gau, M.-J. Li, D. E. Bergles, H. Lu, X. Li, *Nat. Commun.* **2022**, *13*, 1534.
[9] W. Zong, R. Wu, S. Chen, J. Wu, H. Wang, Z. Zhao, G. Chen, R. Tu, D. Wu, Y. Hu, *Nat. Methods* **2021**, *18*, 46.
[10] J. N. Stirman, I. T. Smith, M. W. Kudenov, S. L. Smith, *Nat. Biotechnol.* **2016**, *34*, 857.
[11] C.-Y. Zhong, L. Xiao, J. Zhou, Z. Chen, Y. Chen, Z.-Q. Liu, J. Z. Zhang, *Chem. Eng. J.* **2022**, *431*, 134110.
[12] J. Olesiak-Banska, M. Waszkielewicz, P. Obstarczyk, M. Samoc, *Chem. Soc. Rev.* **2019**, *48*, 4087.
[13] L. Wu, J. Liu, P. Li, B. Tang, T. D. James, *Chem. Soc. Rev.* **2021**, *50*, 702.
[14] B. Ośmiałowski, E. F. Petrusevich, M. A. Antoniak, I. Grela, M. A. Bin Jassar, M. Nyk, J. M. Luis, B. Jędrzejewska, R. Zaleśny, D. Jacquemin, *J. Phys. Chem. Lett.* **2020**, *11*, 5920.
[15] R. Gui, H. Jin, Z. Wang, L. Tan, *Coord. Chem. Rev.* **2017**, *338*, 141.
[16] B. Gidwani, V. Sahu, S. S. Shukla, R. Pandey, V. Joshi, V. K. Jain, A. Vyas, *J. Drug Deliv.* **2021**, *61*, 102308.
[17] J. Lu, M. Tang, T. Zhang, *J. Appl. Toxicol.* **2019**, *39*, 72.
[18] R. W. Epps, M. S. Bowen, A. A. Volk, K. Abdel-Latif, S. Han, K. G. Reyes, A. Amassian, M. Abolhasani, *Adv. Mater.* **2020**, *32*, 2001626.
[19] S. Li, X. Deng, H. Cheng, X. Li, Y. Wan, C. Cao, J. Yu, Y. Liu, Y. Yuan, K. Wang, *ACS nano* **2022**, *16*, 12480.
[20] Q. Zhang, X. Hu, X. Dai, P. Ling, J. Sun, H. Chen, F. Gao, *ACS Nano* **2021**, *15*, 13633.
[21] L. Zhang, Y. Zhou, M. Jia, Y. He, W. Hu, Q. Liu, J. Li, X. Xu, C. Wang, A. Carlsson, *Matter* **2020**, *2*, 1049.
[22] G. Feng, B. Liu, *Acc. Chem. Res.* **2018**, *51*, 1404.
[23] A. Albanese, P. S. Tang, W. C. W. Chan, *Annu. Rev. Biomed. Eng.* **2012**, *14*, https://doi.org/10.1146/annurev-bioeng-071811-150124.
[24] J. Mei, N. L. C. Leung, R. T. K. Kwok, J. W. Y. Lam, B. Z. Tang, *Chem. Rev.* **2015**, *115*, 11718.

[25] Z. Xu, Y. Jiang, Y. Shen, L. Tang, Z. Hu, G. Lin, W.-C. Law, M. Ma, B. Dong, K.-T. Yong, G. Xu, Y. Tao, R. Chen, C. Yang, *Mater. Horiz.* **2022**, *9*, 1283.
[26] S. Chen, H. Wang, Y. Hong, B. Z. Tang, *Mater. Horiz.* **2016**, *3*, 283.
[27] H. M. Kim, B. R. Cho, *Chem. Rev.* **2015**, *115*, 5014.
[28] J. Qi, C. Sun, D. Li, H. Zhang, W. Yu, A. Zebibula, J. W. Y. Lam, W. Xi, L. Zhu, F. Cai, P. Wei, C. Zhu, R. T. K. Kwok, L. L. Streich, R. Prevedel, J. Qian, B. Z. Tang, *ACS Nano* **2018**, *12*, 7936.
[29] X. Deng, Z. Xu, Z. Zhang, W. Zhang, J. Li, L. Zheng, X. Chen, Y. Pan, P. Qiu, D. Wang, *Adv. Funct. Mater.* **2022**, *32*, 2205151.
[30] J. Li, Z. Zhang, X. Deng, Z. Xu, L. Wang, G. Xu, K. Wang, D. Wang, B. Z. Tang, *Biomaterials* **2022**, *287*, 121612.
[31] Z. Xu, Z. Zhang, X. Deng, J. Li, Y. Jiang, W.-C. Law, C. Yang, W. Zhang, X. Chen, K. Wang, *ACS Nano* **2022**, *16*, 6712.
[32] M. Liu, B. Gu, W. Wu, Y. Duan, H. Liu, X. Deng, M. Fan, X. Wang, X. Wei, K.-T. Yong, K. Wang, G. Xu, B. Liu, *Chem. Mater.* **2020**, *32*, 6437.
[33] M. Fan, G. Feng, L. Xia, Y. Zhang, M. Liu, Z. Li, Y. Jiang, C. Yang, W.-C. Law, K.-T. Yong, Y. Shen, Z. Xu, G. Xu, *Adv. Opt. Mater.* **2023**, *11*, 2300255.
[34] Y. Zhou, J. Hua, D. Ding, Y. Tang, *Biomaterials* **2022**, *286*, 121605.
[35] Y. Wang, Y. Qiu, A. Sun, Y. Xiong, H. Tan, Y. Shi, P. Yu, G. Roy, L. Zhang, J. Yan, *Anal. Chim. Acta* **2020**, *1133*, 109.
[36] Y. Tang, D. Zhang, X. Gong, J. Zheng, *Adv. Funct. Mater.* **2022**, *32*, 2208022.
[37] L. Liu, W. Jin, Y. Huang, J. Dai, X. Zheng, Y. Liu, M. Ju, B. Shen, *Sens. Actuators, B* **2022**, *353*, 131098.
[38] X. Chai, H.-H. Han, A. C. Sedgwick, N. Li, Y. Zang, T. D. James, J. Zhang, X.-L. Hu, Y. Yu, Y. Li, Y. Wang, J. Li, X.-P. He, H. Tian, *J. Am. Chem. Soc.* **2020**, *142*, 18005.
[39] Y. Fu, H.-H. Han, J. Zhang, X.-P. He, B. L. Feringa, H. Tian, *J. Am. Chem. Soc.* **2018**, *140*, 8671.
[40] H.-H. Han, A. C. Sedgwick, Y. Shang, N. Li, T. Liu, B.-H. Li, K. Yu, Y. Zang, J. T. Brewster, M. L. Odyniec, M. Weber, S. D. Bull, J. Li, J. L. Sessler, T. D. James, X.-P. He, H. Tian, *Chem. Sci.* **2020**, *11*, 1107.
[41] Z. Liu, X. Chen, *Chem. Soc. Rev.* **2016**, *45*, 1432.
[42] D. Gao, Y. Li, Y. Wu, Y. Liu, D. Hu, S. Liang, J. Liao, M. Pan, P. Zhang, K. Li, *ACS Appl. Mater. Interfaces* **2022**, *15*, 3.
[43] X. Li, M. Zha, Y. Li, J. S. Ni, T. Min, T. Kang, G. Yang, H. Tang, K. Li, X. Jiang, *Angew. Chem., Int. Ed.* **2020**, *59*, 21899.
[44] H. Cong, K. Wang, Z. Zhou, J. Yang, Y. Piao, B. Yu, Y. Shen, Z. Zhou, *ACS Nano* **2020**, *14*, 5887.
[45] W. Yang, C. Xiang, Y. Xu, S. Chen, W. Zeng, K. Liu, X. Jin, X. Zhou, B. Zhang, *Biomaterials* **2020**, *255*, 120186.
[46] P. Cheng, K. Pu, *Nat. Rev. Mater.* **2021**, *6*, 1095.
[47] Z. Yang, Z. Zhang, Z. Lei, D. Wang, H. Ma, B. Z. Tang, *ACS Nano* **2021**, *15*, 7328.
[48] Y. Liu, M. Kong, Q. Zhang, Z. Zhang, H. Zhou, S. Zhang, S. Li, J. Wu, Y. Tian, *J. Mater. Chem. B* **2014**, *2*, 5430.
[49] M. Etinski, J. Tatchen, C. M. Marian, *J. Chem. Phys.* **2011**, *134*, 154105.
[50] S. Gao, G. Wei, S. Zhang, B. Zheng, J. Xu, G. Chen, M. Li, S. Song, W. Fu, Z. Xiao, W. Lu, *Nat. Commun.* **2019**, *10*, 2206.
[51] S. Liu, X. Zhou, H. Zhang, H. Ou, J. W. Y. Lam, Y. Liu, L. Shi, D. Ding, B. Z. Tang, *J. Am. Chem. Soc.* **2019**, *141*, 5359.
[52] Y. Li, Z. Cai, S. Liu, H. Zhang, S. T. H. Wong, J. W. Y. Lam, R. T. K. Kwok, J. Qian, B. Z. Tang, *Nat. Commun.* **2020**, *11*, 1255.
[53] A. Pabbathi, S. Patra, A. Samanta, *ChemPhysChem* **2013**, *14*, 2441.
[54] S. Khatun, *J. Biomol.* **2018**, *36*, 3122.
[55] I. Rombouts, B. Lagrain, K. A. Scherf, M. A. Lambrecht, P. Koehler, J. A. Delcour, *Sci. Rep.* **2015**, *5*, https://doi.org/10.1038/srep12210.
[56] H. Song, Z. Kuang, X. Wang, Y. Guo, Q. Guo, H. Zhang, A. Xia, *J. Phys. Chem. C* **2018**, *122*, 15108.
[57] M. Fan, G. Feng, L. Xia, Y. Zhang, M. Liu, Z. Li, Y. Jiang, C. Yang, W. C. Law, K. T. Yong, *Adv. Opt. Mater.* **2023**, *11*, 2300255.
[58] W. Qin, P. F. Zhang, H. Li, J. W. Y. Lam, Y. J. Cai, R. T. K. Kwok, J. Qian, W. Zheng, B. Z. Tang, *Chem. Sci.* **2018**, *9*, 2705.
[59] D. Ding, C. C. Goh, G. Feng, Z. Zhao, J. Liu, R. Liu, N. Tomczak, J. Geng, B. Z. Tang, L. G. Ng, B. Liu, *Adv. Mater.* **2013**, *25*, 6083.
[60] S. J. Zhen, S. W. Wang, S. W. Li, W. W. Luo, M. Gao, L. G. Ng, C. C. Goh, A. J. Qin, Z. J. Zhao, B. Liu, B. Z. Tang, *Adv. Funct. Mater.* **2018**, *28*, 1706945.
[61] S. W. Wang, F. Hu, Y. T. Pan, L. G. Ng, B. Liu, *Adv. Funct. Mater.* **2019**, *29*, 1902717.
[62] Y. Y. Li, S. J. Liu, H. W. Ni, H. Zhang, H. Q. Zhang, C. Chuah, C. Ma, K. S. Wong, J. W. Y. Lam, R. T. K. Kwok, J. Qian, X. F. Lu, B. Z. Tang, *Angew. Chem., Int. Ed.* **2020**, *59*, 12822.
[63] Z. Zheng, D. Y. Li, Z. Y. Liu, H. Q. Peng, H. H. Y. Sung, R. T. K. Kwok, I. D. Williams, J. W. Y. Lam, J. Qian, B. Z. Tang, *Adv. Mater.* **2019**, *31*, 1904799.
[64] Z. Zheng, T. Y. Yang, D. Y. Li, H. Cao, J. Y. Gong, H. X. Liu, C. C. Zhou, L. J. Liu, P. F. Wei, X. G. Gu, P. Lu, J. Qian, B. Z. Tang, *ACS Nano* **2023**, *17*, 8782.
[65] S. Samanta, M. N. Huang, S. Q. Li, Z. G. Yang, Y. He, Z. Y. Gu, J. G. Zhang, D. Zhang, L. W. Liu, J. L. Qu, *Theranostics* **2021**, *11*, 2137.
[66] Z. R. Xu, X. Q. Deng, G. Feng, W. J. Zhang, Y. B. Zhang, W. G. Zhang, M. Z. Fan, M. N. Hu, C. B. Yang, M. Ying, Y. Y. Shen, W. X. Xie, K. Wang, G. X. Xu, *Chem. Eng. J.* **2023**, *465*, 142850.
[67] S. W. Wang, J. Liu, C. C. Goh, L. G. R. Ng, B. Liu, *Adv. Mater.* **2019**, *31*, 1904447.
[68] J. Qi, C. W. Sun, D. Y. Li, H. Q. Zhang, W. B. Yu, A. Zebibula, J. W. Y. Lam, W. Xi, L. Zhu, F. H. Cai, P. F. Wei, C. L. Zhu, R. T. K. Kwok, L. L. Streich, R. Prevedel, J. Qian, B. Z. Tang, *ACS Nano* **2018**, *12*, 7936.
[69] M. Paar, V. H. Fengler, D. J. Rosenberg, A. Krebs, R. E. Stauber, K. Oettl, M. Hammel, *Commun. Biol.* **2021**, *4*, 731.
[70] N. Punyaratabandhu, P. Dechadilok, W. Triampo, P. Katavetin, *Microcirculation* **2022**, *29*, e12779.